Southern Ocean surface pressure and winds during the 20th century from proxy-data assimilation

Gemma O'Connor (goconnor@uw.edu)
University of Washington
Eric Steig
University of Washington https://orcid.org/0000-0002-8191-5549
Gregory Hakim
University of Washington https://orcid.org/0000-0001-8486-9739

Article

Keywords: paleoclimate, cyrospheric science, climate change

Posted Date: February 9th, 2021

DOI: https://doi.org/10.21203/rs.3.rs-151209/v1

Abstract

Winds and pressure over the Southern Ocean are critical to many aspects of the climate system, including ocean circulation and carbon uptake, sea ice extent, and the mass balance of Antarctica. However, reliable climate data around Antarctica begin only in 1979. Here, we reconstruct sea level pressure and zonal surface wind anomalies over the Southern Ocean through the 20th century, using data assimilation with a global database of paleoclimate proxy records. There is very good agreement between the reconstructions and satellite-based reanalysis products both at the large scale and in the smaller Amundsen Sea, a key region of West Antarctica where rapid glacier retreat has occurred in recent decades. The reconstructions show insignificant trends in the zonal-average circumpolar westerlies, but a significant strengthening in mid-latitude Pacific westerlies, associated with a deepening of the Amundsen Sea Low, beginning well before the satellite era. The mean zonal-wind trend along the continental shelf break in the Amundsen Sea is easterly through the 20th century, contrasting with previous results that have suggested that glacier change in this region can be attributed to strengthening westerlies. Our reconstructions underscore the value of using paleoclimate data assimilation methods in assessing historical changes in Southern Hemisphere climate and suggest that zonally asymmetric features of atmospheric circulation may be key for understanding high-latitude climate and associated ice-sheet changes.

1. Introduction

Winds over the Southern high latitudes play a pivotal role in the global heat and carbon budget through their influence on air-sea exchange and vertical convection in the Southern Ocean[1,2]. Winds also play a significant role in sea ice variability[3,4] and in modulating the distribution of water masses that affect the delivery of heat to the margin of the Antarctic Ice Sheet, potentially affecting ice sheet stability[5,6].

Much attention has been paid to changes in the large-scale westerlies, which have strengthened and may have shifted poleward in recent decades[7,8]. Such changes are commonly expressed as a positive trend in the Southern Annular Mode (SAM) index, a measure of the zonal mean difference in high *vs.* mid-latitude pressure around the Southern Ocean[9]. It is also important to consider the spatial pattern of atmospheric circulation changes[10,11]. For example, it has been suggested that the intensification of the large-scale circumpolar winds may explain the widespread increase of ice discharge in Antarctica[12], because wind-driven incursions of Circumpolar Deep Water (CDW) onto the continental shelf enhance the melting of floating ice shelves[5,13]. Yet, the largest changes in climate have occurred in the relatively small region of West Antarctica, where zonally asymmetric features of atmospheric circulation are more important[14]; wind variability in this region is uncorrelated with the SAM index[15].

The greatest increases in ice discharge have occurred in the Amundsen Sea region of West Antarctica[6]. Wind variability in this region is associated with the Amundsen Sea Low (ASL), which is strongly influenced by the El Niño/ Southern Oscillation (ENSO) in the tropical Pacific[15,16,17]. Large ENSO events

have a demonstrated impact on the flow of CDW onto the continental shelf[18], but it is not clear that tropical forcing can account for the increasing ice discharge that has evidently occurred through the 20th century. This has led to the suggestion, supported by climate-model simulations, that interannual wind variability in the Amundsen Sea region, while dominated by tropical forcing, is superimposed on a long-term westerly trend driven by radiative forcing[19].

A challenge to understanding how Southern Ocean wind and associated pressure fields have affected the ocean and cryosphere is that neither is well documented prior to the satellite era (i.e., before 1979). Global atmospheric reanalyses and other gridded products of wind and pressure that span the 20th century[20,21,22] show large inconsistencies with one another at high southern latitudes[23] and are known to be particularly uncertain in the critical West Antarctic sector[21].

Advances in data assimilation methods using paleoclimate proxy records provide an opportunity to improve our understanding of wind and pressure changes at the high latitudes, where instrumental data are often sparser than proxy data. A well-established method, which employs the ensemble Kalman filter, has been used to reconstruct a range of variables, including precipitation, geopotential height, and sea ice, and has proven to be competitive with instrumental reanalyses[24,25,26].This approach blends temporal information from temperature-sensitive proxy records with spatial covariance information from climate models, used as the prior ensemble. It relies on comparison between the temperature field in the prior ensemble with the proxy data, which are calibrated against instrumental temperature records, accounting for uncertainties in both. Here, we use this method to reconstruct gridded anomalies of annual-mean sea level pressure (SLP) and zonal surface winds (U_S) from 1900 through 2005, as these are the most relevant variables to the oceanographic and glacier changes occurring around Antarctica (Methods). We also reconstruct surface temperature. We assess the skill of our reconstructions by comparing them to instrumental reanalysis products and other proxy-based reconstructions using standard metrics (Methods). We discuss trends in the data over recent decades, and the full 20th century, in the context of climate and glaciological applications. We consider both the large-scale changes relevant to the response of high latitude climate to radiative forcing, and the regional changes relevant to Antarctica, with particular attention to the Amundsen Sea region.

2. Results

2.1 Verification and comparison with instrumental reanalyses

We discuss two main reconstructions generated from assimilation of proxy records with two different last millennium climate model priors, from the Community Earth System Model ("CESM"[27]) and the Hadley Centre Coupled Model, version 3 ("HadCM3"[28]). We evaluate our results by comparing SLP and U_S reconstructions with the established instrumental reanalysis products ERA5[29] and NCEP2[30]. Maps of the correlation (*r*) and coefficient of efficiency (*CE*) between our reconstructions and the instrumental reanalyses during the satellite era (since 1979) indicate very good skill (correlation *p*-values < 0.05, *CE* > 0)

for SLP and U_S over most of the Southern Hemisphere (Figs. 1, S1, S2). For both variables, skill is greatest in the Pacific sector of the Southern Ocean, reflecting the density of ice-core proxy data near this region and the strong teleconnections between the West Antarctic and lower latitudes[17,31]. Correlation and *CE* tend to be slightly greater in the reconstruction that uses CESM as the prior, than in the reconstruction using HadCM3.

Our reconstructions reproduce both the magnitude and spatial pattern of trends in annual-mean SLP and U_S that are observed in ERA5 and NCEP2 (Fig. S3). All show the large-scale pattern characteristic of the well-known increase in the SAM index[32]: increasing SLP at mid latitudes, decreasing SLP poleward of ~ 50°S, and stronger mid-latitude westerlies. Our reconstructions also capture the deepening of the ASL that has been noted in recent decades[33] and is documented in HADSLP2[34] data since 1951[11] (Fig. 2). HadSLP2, which uses surface observations only (i.e., no satellite data), was produced with an interpolation procedure independent of the reanalyses products. As in HADSLP2, ASL deepening since the 1950s in our reconstructions is accompanied by increasing SLP over the Drake Passage, a pattern that has also been noted in previous work[35].

Our reconstructions also reproduce the well-established warming trend over the Antarctic Peninsula and the West Antarctic Ice Sheet since the 1950s, and insignificant trends over East Antarctica (Fig. S4), comparing well with independent statistical reconstructions[14,36]. This pattern of warming and cooling in Antarctica is consistent with the SLP trends[14,37,38]. Reconstructions obtained with and without ice core data show that these temperature and SLP patterns are derived predominantly from the ice-core proxy data, particularly the snow-accumulation records. Previous work has noted that Antarctic accumulation records provide a strong constraint on temperature[39]. Reconstructions conducted with the direct assimilation of $\delta^{18}O$ data (i.e., independent of calibration against instrumental temperature data) produce similar temperature, SLP and U_S patterns, though the trends are comparatively damped (Fig. S4). Hence, both ice-core accumulation and $\delta^{18}O$ records play an important role in our data assimilation results. Indeed, reconstructions without ice cores show a trend toward increasing pressure in the Amundsen Sea, opposite to that in the HADSLP2 observations.

2.2 Large-scale SLP and wind trends during the 20th century

As noted in the previous section, our reconstructions reproduce the SLP and zonal-wind trends during the satellite era that are commonly associated with an increase in the SAM index. Here, we consider trends over the full 20th century by calculating the SAM index from our reconstructions using the difference in zonal average SLP between 65°S and 40°S (Fig. S5). Our results compare well (correlation *p*-values < 0.05, Table S2) with the instrumental Marshall SAM index[9] as well as with a previously published 1000-year-long reconstruction of the SAM index[40] (calculated with a weighted composite of Antarctic ice-core and South American tree-ring data). Consistent with previous work, our results show a weak positive trend in the SAM Index earlier in the 20th century and a stronger positive trend late in the 20th century (Table S2). Correlations with the Marshall SAM index and the Abram index are poor if ice-core data are excluded (Table S2), again highlighting the important contribution from ice cores.

An increase in the SAM index is associated in the literature with a combination of the strengthening and poleward shift of the polar jet and surface westerlies[41]. We quantify the Southern Hemisphere (SH) surface westerly position as the latitude of the center of mass of U_s between 20°S and 70°S (Methods). The SH surface westerly strength is the wind speed at that same latitude. We perform these calculations for both the circumpolar average and by sector (Pacific, Atlantic, and Indian; Fig. 3). We find excellent agreement in interannual variability between the reconstructions and results of the same calculations for instrumental reanalysis products for the period 1979–2005, for both circumpolar position and strength (Table S2). We note that the reconstructions may inherit mean biases from their priors, but we find only small biases in the reconstructions relative to ERA5 and NCEP2 (Methods, Table S4).

In our reconstructions of SH westerly wind position from 1979–2005, there is a more equatorward trend in the Pacific sector than in the zonal average, though associated with large uncertainties (Fig. 3). Similarly, previous work shows inconclusive trends in annual mean SH westerly position since 1979[8], with contrasting regional trends[42]. Our results show that there is no significant trend (Methods) in annual mean position for the full 20th century, and that contrasting regional trends started well before the satellite era (Table S3). This indicates that SH westerly position is subject to large variability, and trends associated with short datasets should be interpreted with caution.

For SH westerly wind strength, reconstructed trends for 1979–2005 agree well with those in ERA5 and are weaker than those in NCEP2. We find greatest strengthening in the Pacific and Indian sectors, consistent with ERA5 and NCEP2, and weakest signs of strengthening in the Atlantic. For the period 1900 to 2005, the reconstructions show a small increase in the circumpolar SH westerlies of 0.09 ± 0.21 m/s/century and 0.23 ± 0.18 m/s/century (reported errors are ± 2 standard deviations; see Methods). We find more robust strengthening in the Pacific, with significant trends of 0.64 ± 0.36 m/s/century and 0.52 ± 0.26 m/s/century. Pre-satellite era trends reveal similar strengthening, indicating that weak circumpolar strengthening and significant Pacific strengthening started well before the satellite era.

We also compare our results with two additional instrumental reanalysis products, 20CRv3[22] and ERA20C[20], which extend through the full 20th century. Both show a significant poleward shift and strengthening of the zonal surface winds during the full 20th century, with much larger trends than our reconstructions indicate (Table S4). The greatest differences in these 20th century instrumental reanalyses lie in the first half of the century (Fig. S6), which is not surprising given that both 20CRv3 and ERA20C are largely unconstrained by high-latitude observations prior to the satellite era. Our results – which are constrained by high-latitude observations throughout the entire 20th century – thus support previous work suggesting that the zonal wind and pressure trends in 20th century instrumental reanalysis products are spuriously large[11].

2.3. Wind and pressure trends during the 20th century in the Amundsen Sea region

As noted above, a distinct feature of our reconstructions is deepening of the Amundsen Sea Low and increasing pressure over the Drake Passage (Fig. 2). This zonally asymmetric pattern persists through the 20th century in our reconstructions (Fig. 4), contrasting with the 20CRv3 and ERA20C instrumental

reanalysis products, as well as with climate-model simulations, which tend to show more annular, zonally symmetric strengthening of the circumpolar westerlies (Fig. S8). Both of our reconstructions show similar patterns in the Amundsen Sea region; areas of disagreement are largely restricted to the East Antarctic sector, where verification skill is lowest and there are the fewest observational constraints (Figs. 1, S1, S2). The pressure pattern in the Amundsen Sea is associated and physically consistent with the westerly wind trend evident in the mid-latitude Pacific, as well as an easterly trend along the Antarctic coastline.

Pressure and wind changes in the small region of the Amundsen Sea Embayment, close to the Antarctic continent, are of particular interest. The zonal winds along the continental shelf break (70–72°S, 102–114°W) provide a useful index of the processes relevant to wind-driven changes associated with glacier retreat[5,18]. Our reconstructions of SLP in this region show excellent agreement with instrumental reanalyses (Figs. 5, S9, Table S2). For winds, agreement with ERA5 is good, but is poor with NCEP2; we note that independent assessments have concluded that ERA Interim (the previous generation of the ERA5 product), is the most accurate product for Amundsen Sea winds[43]. For our reconstructions, the mean zonal wind trend for the period 1900 to 2005 is easterly; this is accompanied by a negative pressure trend. These trends are all statistically significant (Table S2), and the sign of these trends is robust to the use of different proxy types (e.g., with and without the ice core data) (Fig. S10).

3. Discussion

The reconstructions presented here extend the record of sea level pressure and surface winds over the Southern Ocean through the 20th century, constrained by high-latitude proxy observations. There is very good agreement with instrumental reanalyses during the period of overlap, 1979–2005, at both large and regional scales. Trends in the SH surface westerlies during the satellite era are similar to satellite-based reanalyses, within uncertainties, and the patterns of longitudinal variation have been seen in previous work[42] and other reanalysis products, such as MERRA[44] and JRA55[45]. We emphasize that while our reconstructions are limited to annual-mean only, instrumental reanalyses and climate models show statistically significant poleward shifts since 1979 only during the austral summer, counteracted by equatorward shifts during the austral spring[8]. Thus, the annual mean trend is weak, and generally not statistically significant, as our reconstructions show. Our results do not support the strong 20th century trends suggested by the 20CRv3 or ERA20C instrumental reanalyses in either SH westerly wind position or strength. We do, however, find significant strengthening of the surface westerlies in the Pacific sector throughout the 20th century. This strengthening is closely related to the deepening of the ASL, which is statistically significant for the full period of our reconstruction (1900–2005, Table S2), and has been observed in independent analyses since the 1950s[11].

Our results have implications for the role of radiative forcing in driving atmospheric circulation changes at high southern latitudes over the 20th century. While strengthening and poleward-shifting SH westerlies during the austral summer are associated with increasing greenhouse gases and stratospheric ozone depletion[46,47,42], longitudinal variations in position can be attributed to natural variability[42], suggesting

that the insignificant trends in 20th century position observed here may be a result of large internal variability. However, the strengthening mid-latitude westerlies in the Pacific sector may be associated with increased greenhouse gases, as this is a feature found in historical simulations with increased CO_2 forcing[42].

Our results also have implications for our understanding of the relationship between climate and glacier change in West Antarctica. In particular, a recent study suggested that there has been a mean westerly trend in zonal winds along the continental shelf break in the Amundsen Sea through the 20th century[19], which could explain the increased ice discharge in this region. That study[19] used climate simulations from a "tropical pacemaker" climate-model ensemble ("PACE"), in which fully coupled-runs of CESM1.1 were constrained to follow observed tropical sea surface temperatures[48], but are unconstrained in the extratropics. In our reconstructions, the mean 20th century trend in this region is easterly. This difference is not an artifact of our reconstruction method: we conducted a "pseudoproxy" experiment, in which we sample the PACE temperature field at the locations of real proxy data and use these to reconstruct the known climate model history (Methods). Both the interannual variability and trends in the Amundsen Sea are faithfully reproduced (Figs. S11, S12). Thus, the discrepancy between our findings and those in PACE for winds in the Amundsen Sea may be related to the simulation of the ASL in climate models. Historical climate model simulations for the 20th century, including PACE, generally do not show the ASL deepening seen in our reconstructions (Figs. S8, S12). Previous work has noted that the ASL is poorly represented in climate models, probably because of inadequate resolution of the Antarctic topography[49,50]. Because the ASL is associated with meridional flow that affects winds around West Antarctica[51,10], it is thus not surprising that climate models may not adequately simulate historical wind changes at the regional scale in the Amundsen Sea.

Changing winds have almost certainly played a leading role in the enhanced intrusion of CDW onto the continental shelf in the Amundsen Sea, and elsewhere in Antarctica, driving Antarctic ice-sheet mass loss[12], but our results show that relatively simple mechanisms like increasing westerlies along the continental shelf break[19] do not provide an adequate explanation. Instead, glacier change in Antarctica may have been initiated by specific westerly wind events, such as are associated with the very strong 1939–1942 El Niño[52,15,53], or by changes in event frequency associated with changes in the intensity of ENSO activity in recent decades[54,55]. Alternatively, the properties of CDW on the continental shelf may be more strongly affected by changes in the large-scale circumpolar westerlies, well to the north of the continental shelf[56] than has been suggested by previous work focused primarily at the regional scale[13].

Our reconstructions underscore the value of using paleoclimate data assimilation methods in assessing historical changes in climate, especially in the high latitudes of Southern Hemisphere where instrumental data constraints are sparse. Our results also support other work that suggests that climate models may not adequately simulate higher-order patterns of atmospheric circulation variability such as the Amundsen Sea Low[50], and suggest that simulations such as the PACE ensemble may produce a simpler, more annular circumpolar westerly strengthening through the 20th century than has occurred in reality.

Such limitations should be considered when considering projections of high latitude climate, and associated ice-sheet changes, in the coming centuries.

Methods

Data assimilation method. The reconstructions are generated using the ensemble Kalman filter to spatially spread information from global paleoclimate proxy data using teleconnection patterns captured by covariance structures in climate models, following the Last Millennium Reanalysis framework[25,26]. The ensemble approach generates a distribution of climate states, allowing us to estimate the most probable state as well as quantify associated errors. Additionally, this approach can generate multiple climate fields at once, including those not typically derived from proxy data. We use an offline data assimilation method in which we randomly draw annually-averaged anomaly states from climate model output to form a prior ensemble with 100 members, which we use for every year reconstructed. This approach ensures that the temporal variance and trends in the final reconstruction, or “posterior” ensemble, are generated from the proxies rather than variability in the model. This approach also leaves us with a posterior ensemble of 100 members, which we use to calculate uncertainty. Additionally, the offline approach allows us to test the sensitivity of the reconstruction to the choice of climate model used for the prior.

Our ensemble data assimilation method follows these equations:

Our ensemble data assimilation method follows these equations:

$$\boldsymbol{x}^a = \boldsymbol{x}^p + \boldsymbol{K}[\boldsymbol{y} - H(\boldsymbol{x}^p)] \quad (1)$$

$$\boldsymbol{K} = \boldsymbol{B}\boldsymbol{H}^T[\boldsymbol{H}\boldsymbol{B}\boldsymbol{H}^T + \boldsymbol{R}]^{-1} \quad (2)$$

where $\boldsymbol{x}^a$ is the posterior analysis state vector, or the reconstructed climate state. We form the prior, $\boldsymbol{x}^p$, by drawing 100 random climate states from climate model output. We use two climate models to produce the two reconstructions: the iCESM Last Millennium Ensemble[28] and the HadCM3 Last Millennium Ensemble[29]. We assimilate proxy observations, $\boldsymbol{y}$, in the innovation term, $[\boldsymbol{y} - H(\boldsymbol{x}^p)]$, where $H(\boldsymbol{x}^p)$ is the prior estimate mapped to proxy space using a forward model. We use proxies from a database consisting of the PAGES 2k records[57], additional ice core accumulation records[58], and additional coral records[59]. The amount of weight that the innovation gets is determined by $\boldsymbol{K}$, the Kalman gain (equation 2). $\boldsymbol{K}$ is primarily dependent on the covariance structure from the prior, $\boldsymbol{B}$, and the observational error in the proxy, $\boldsymbol{R}$. We quantify the error for each proxy record as the variance of the regression residuals from the forward model.

The forward model used to map the prior estimate to proxy space is a seasonal linear regression between instrumental temperature anomalies and each proxy record for the period of overlap. For tree-ring records, we use a seasonal bilinear forward model calibrated to both instrumental temperature and precipitation data with proxy-specific seasonality[26]. Our calibration data for temperature and precipitation are GISTEMP[60] and Global Precipitation Climatology Centre[61] (GPCC), respectively. For ice core records from Antarctica, we calibrate the data to temperatures from Nicolas and Bromwich, 2014 rather than GISTEMP. Nicolas and Bromwich, 2014 is the most up to date and accurate spatial temperature reconstruction for Antarctica, though we note that the reconstructions show only very minor differences if we calibrate the ice cores to GISTEMP. The ice core records we use comprise both water-isotope ($\delta^{18}O$) records and annual-accumulation records; both are calibrated to temperature, following a study[39] that found that using both accumulation and $\delta^{18}O$ yields better performance for temperature than reconstructions using $\delta^{18}O$ alone. GPCC is not reliable over Antarctica, and while other precipitation data sets are available, climate models generally show significant bias in accumulation; we therefore do not use an accumulation prior.

The anomaly reference period in the reconstructions is 1961-1990 unless otherwise noted (e.g., in comparisons to satellite-based reanalysis products that start in 1979, in which we shift the anomaly reference period in the reconstructions by moving them by the difference in reconstruction mean from 1961-1990 and 1979-2005). The reconstructions are regridded to 1° resolution.

Correlation and coefficient of efficiency calculations. To assess reconstruction skill, we calculate correlation to measure signal timing (after accounting for autocorrelation) and coefficient of efficiency to quantify errors in signal amplitude or bias. We use the Pearson correlation coefficient to calculate correlation on the ensemble mean time series. Correlation significance is calculated with the 2-tailed student t-test with 95% confidence, using the number of independent samples (N) that accounts for autocorrelation[62]:

$$N = N_{samples} \times \left(\frac{1 - r_x r_y}{1 + r_x r_y}\right) \quad (3)$$

where r_x and r_y are the lag-1 autocorrelations of time series x and time series y. We calculate the coefficient of efficiency[63] as:

$$CE = 1 - \left(\frac{\sum_{i=1}^{n}(v_i - x_i)^2}{\sum_{i=1}^{n}(v_i - \bar{v})^2}\right) \quad (4)$$

where v = verification values and x = reconstruction values.

Calculations of trend magnitude and uncertainty. Trends are calculated as the slope of a linear regression for the ensemble mean of the reconstruction. To calculate uncertainty on the magnitude of the trend, we randomly draw from the 100 ensemble members for each year to generate a random ensemble of time series (i.e., the ensemble indices are randomly labeled in time). We perform this step 100 times and calculate the uncertainty as twice the standard deviation of the 100 linear fits associated with these random draws. We note that 100 is sufficient for the statistics to converge. We use 2σ as the uncertainty bounds on the magnitude of the trend, as the data these are performed on are approximately normal (by failing to reject a Kolmogorov-Smirnov test for normality with 95% confidence). Thus, 2 standard deviations from the mean is equivalent to the middle 95% of the 100-member ensemble trends.

Trend significance. Trends are considered statistically significant if two criteria are met: (1) the trend magnitudes and their uncertainties for both reconstructions overlap with each other and do not overlap with 0 (i.e. they are consistent in sign and magnitude), and (2) if the 95% confidence intervals of the ensemble mean trend do not overlap with 0, after accounting for autocorrelation, in both reconstructions (i.e. how meaningful the linear trend is for how noisy the data are). The 95% confidence interval of the linear fit (for the second criteria) is calculated as follows:

$$\hat{b} - t_{\alpha}^{N-2}\hat{\sigma}_b < b < \hat{b} + t_{\alpha}^{N-2}\hat{\sigma}_b \quad (5)$$

where b = the linear trend, σ = the sample standard deviation of the residual, α = 0.05, and N = the number of independent samples that accounts for the lag-1 autocorrelation of the time series, calculated using equation 3.

Southern hemisphere surface westerly position and strength calculations. We calculate the circumpolar Southern Hemisphere (SH) westerly wind position as the center of mass latitude for zonally averaged westerly winds between the latitudes of 20°S and 70°S. The SH surface wind strength is the wind speed at the center of mass latitude. To perform these calculations, we add the mean of the prior back into the respective reconstruction so that we are working with the full climate field. Trends are calculated with 100 randomly generated time series drawn from ensemble members following the steps outlined above. We perform this calculation on the zonal average (full circumpolar) and by regions[64]: the Pacific (150–290°E), Atlantic (290–20°E), and Indian (20–150°E) Ocean regions (Table S3).

Model bias in the reconstructions. The trends in the reconstructions are generated by information from the proxies, but the mean wind speeds and wind positions are largely inherited from the models that the priors are drawn from (Fig. S7, Table S4). As a result, the CESM reconstruction shows a positive bias in wind strength (1.19 m/s) relative to ERA5, while the HadCM3 reconstruction shows a negative bias relative to NCEP2 (-1.19 m/s). The reconstructions show minor position biases relative to both ERA5 and NCEP2 (-0.43° to 0.86°). These biases are small compared to biases seen across CMIP5 and CMIP6 models[50]. Wind position biases in models have been shown to affect trends in the circumpolar westerly wind position[64,65,66], so trends subject to biases must be treated with caution. However, even with contrasting biases in strength and small biases in position, both reconstructions show insignificant trends in position and weak strengthening of the SH westerlies during the 20th century, with a large strengthening component from the Pacific region.

Pseudoproxy experiments. We use the same data assimilation method as the real-proxy reconstructions to generate pseudoproxy reconstructions, with a few changes. We use a prior from a historical model so that we can generate pseudoproxies from the 20th century. We use a PACE prior composed of ensemble members 2-20, concatenated together to form a sufficiently long list of climate states to draw from. We generate the pseudoproxies by drawing temperature from the proxy locations in ensemble member 1 of PACE. Since the pseudoproxies are taken directly from the temperature fields, no forward model is needed. We use an observational error of 0.01°C. The ability of the pseudoproxy reconstructions to reproduce the historical climate models allows us to understand the upper bound of how well our method can reproduce the truth, given the proxy locations that we have and the covariance structures in the models.

Declarations

Acknowledgements

The authors thank Robert Tardif for help with code development and the Last Millennium Reanalysis group at the University of Washington for helpful discussions and support. GKO was supported by the National Science Foundation (NSF) Graduate Research Fellowship Program and the Achievement Rewards for Collegiate Scientists fellowship. GJH acknowledges support from NSF (grant AGS-1702423) and Heising-Simons Foundation (grant 2016-014). EJS acknowledges support from NSF (grant ARCSS-1503281).

Author contributions

GKO and EJS designed the study. GKO generated the paleoclimate reconstructions, performed the analyses, and wrote the first draft of the paper. EJS provided guidance on reconstruction methods and analyses and made significant revisions to the paper. GJH provided guidance on data assimilation methodology, statistics, and interpretation of results. All authors contributed to the final version of the paper.

Competing interests

The authors declare no competing interests.

References

1. Russell, J. L. et al. The Southern Hemisphere Westerlies in a Warming World: Propping Open the Door to the Deep Ocean. *J. Clim.* **19***,* 6382-6390 (2006).
2. Marshall, J. and Speer, K. Closure of the meridional overturning circulation through Southern Ocean upwelling. *Nat Geosci.* **5,** 171-180 (2012).
3. Kwok, R., and Comiso, J. C. Southern Ocean climate and sea ice anomalies associated with the Southern Oscillation, *J. Clim.*, **15** (3), 487–501 (2002).
4. Kwok, R., Comiso, J. C., Lee, T., Holland, P. R. Linked trends in the South Pacific sea ice edge and Southern Oscillation Index. *Geophys. Res. Lett.* **43,** 10,295–10,302 (2016).
5. Thoma, M., Jenkins, A., Holland, D. & Jacobs, S. Modelling Circumpolar Deep Water intrusions on the Amundsen Sea continental shelf, Antarctica. *Geophys. Res. Lett.* **35,** L18602 (2008).
6. Jenkins, A. et al. Observations beneath Pine Island Glacier in West Antarctica and implications for its retreat. *Nat. Geosci.* **3,** 468–472 (2010).
7. Yin, J.H. A consistent poleward shift of the storm tracks in simulations of 21st century climate. *Geophys. Res. Lett.* **32,** L18701 (2005).
8. Swart, N. and Fyfe, J. C. Observed and simulated changes in the Southern Hemisphere surface westerly wind-stress. *Geophys. Res. Lett.* **39,** L16711 (2012).

9. Marshall, G. J. Trends in the Southern Annular Mode from observations and reanalyses. *J. Clim.* **16,** 4134–4143 (2003).
10. Hosking, J., Orr, A., Marshall, G., Turner, J., Phillips, T. The influence of the Amundsen-Bellingshausen Seas Low on the climate of West Antarctica and its representation in coupled climate model simulations. *J. Clim.* **26,** 6633-6648 (2013).
11. Swart, N. C., Fyfe, J. C., Gillett, N., Marshall, G. J. Comparing Trends in the Southern Annular Mode and Surface Westerly Jet. *J. Clim.* **28,** 8840-8859 (2015).
12. Pritchard, H. D. et al. Antarctic ice-sheet loss driven by basal melting of ice shelves. *Nature* **484,** 502–505 (2012).
13. Jenkins, A. et al. Decadal ocean forcing and Antarctic Ice Sheet response: lessons from the Amundsen Sea. *Oceanography* **29,** 106–117 (2016).
14. Steig, E. J. et al. Warming of the Antarctic ice-sheet surface since the 1957 International Geophysical Year. *Nature* **457,** 459–462 (2009).
15. Steig, E. J., Ding, Q., Battisti, D. S. & Jenkins, A. Tropical forcing of Circumpolar Deep Water inflow and outlet glacier thinning in the Amundsen Sea Embayment, West Antarctica. *Ann. Glaciol.* **53,** 19–28 (2012).
16. Lachlan-Cope, T. & Connolley, W. Teleconnections between the tropical Pacific and the Amundsen–Bellinghausens Sea: role of the El Niño/Southern Oscillation. *J. Geophys. Res. Atmos.* **111,** D23101 (2006).
17. Ding, Q., Steig, E. J., Battisti, D. S. & Küttel, M. Winter warming in West Antarctica caused by central tropical Pacific warming. *Nature Geosci.* **4,** 398–403 (2011).
18. Dutrieux, P. et al. Strong sensitivity of Pine Island ice-shelf melting to climatic variability. *Science* **343,** 174–178 (2014).
19. Holland, P. R., et al. West Antarctic ice loss influenced by internal climate variability and anthropogenic forcing. *Nat geosci.* **12**, 718-724 (2019).
20. Poli, R. et al. ERA-20C: An Atmospheric Reanalysis of the Twentieth Century. *J. Clim.* **29** (11), *4083–4097* (2016).
21. Fogt, R. L., et al., Antarctic station-based seasonal pressure reconstructions since 1905: 1. Reconstruction evaluation, *J. Geophys. Res. Atmos.*, **121**, 2814– 2835 (2016).
22. Slivinski, L.C. et al., Towards a more reliable historical reanalysis: Improvements for version 3 of the Twentieth Century Reanalysis system. *Quart. J. Royal Met. Soc.* **145** (724), 2876– 2908 (2019).
23. Wohland, J., Omrani, N. E., Witthaut, D., and Keenlyside, N. S. Inconsistent wind speed trends in current twentieth century reanalyses. *J. Geophys. Res. Atmos.* **124,** 1931–1940 (2019).
24. Hakim, G. J. et al., The last millennium climate reanalysis project: Framework and first results. *J. Geophys. Res. Atmos.* **121,** 6745-6764 (2016).
25. Tardif, R. et al., Last Millennium Reanalysis with an expanded proxy database and seasonal proxy modeling. *Clim. Past,* **15** (4), 1251–1273 (2019).

26. Brennan, M. K., Hakim, G. J., & Blanchard-Wrigglesworth, E. Arctic sea-ice variability during the instrumental era. *Geophysical Research Letters*, **47,** e2019GL086843 (2020).
27. Brady, E. et al. The Connected Isotopic Water Cycle in the Community Earth System Model Version 1. *J. Adv. Model. Earth Sys.* **11** (8), 2547-2566 (2019).
28. Collins, M., Tett, S. F. B., Cooper, C. The internal climate variability of HadCM3, a version of the Hadley Centre coupled model without flux adjustments. *Clim. Dyn.* **17,** 61-81 (2001).
29. Hersbach, H., B. Bell, P. Berrisford Hirahara, S., Horányi, A., Muñoz-Sabater, J., Nicolas, J., Peubey, C., Radu, R., Schepers, D. and Simmons, A. The ERA5 Global Reanalysis. *Quart. J. Royal Met. Soc.*, **146** (730), 1999-2049 (2020).
30. Kanamitsu, M. NCEP–DOE AMIP-II Reanalysis (R-2). *Bull. Amer. Meteor. Soc*. **83** (11), 1631–1644 (2002).
31. Steig, E. J. et al. Recent climate and ice-sheet changes in West Antarctica compared with the past 2,000 years. *Nat. Geosci*. **6,** 372–375 (2013).
32. Thompson, D. W. J. and Solomon, S. Interpretation of recent Southern Hemisphere climate change. *Science*, **296,** 895–899 (2002).
33. Raphael, M. N. et al. The Amundsen Sea Low: variability, change, and impact on Antarctic climate. *Bull. Am. Meteorol. Soc*. **97,** 111–121 (2016).
34. Allan, R., and Ansell, T. A new globally complete monthly historical gridded mean sea level pressure dataset (HadSLP2): 1850–2004. *J. Climate*, **19,** 5816–5842 (2006).
35. Raphael, M. N., Holland, M. M. Twentieth century simulation of the southern hemisphere climate in coupled models. Part 1: large scale circulation variability. *Clim. Dyn.* **26,** 217-228 (2006).
36. Nicolas, J. P. and Bromwich, D. H. New Reconstruction of Antarctic Nera-Surface Temperature: Multidecadal Trends and Reliability of Gloabl Reanalyses. *J. Clim.* **27,** 8070-8093 (2014).
37. Schneider, D. P., Deser, C., Okumura, Y. An assessment and interpretation of the observed warming of West Antarctica in the austral spring. *Clim. Dyn.* **38,** 323-347 (2012).
38. Bromwich, D. H., et al. Central West Antarctica among the most rapidly warming regions on Earth. *Nat. Geosci.* **6,** 139-145 (2013).
39. Dalaiden, W. et al. How useful is snow accumulation in reconstructing surface air temperature in Antarctica? A study combining ice core records and climate models. *The Cryosphere.* **14,** 1187-1207 (2020).
40. Abram, N. J. et al. Evolution of the Southern Annular Mode during the past millennium. *Nat. Clim. Change* **4,** 564–569 (2014).
41. Previdi, M. and Polvani, L. M. Climate system response to stratospheric ozone depletion and recovery. *Quart. J. Roy. Met. Soc.* **140,** 2401-2419 (2014).
42. Waugh, D. W., Banerjee, A., Fyfe, J. C., Polvani, L. M. Contrasting Recent Trends in Southern Hemisphere Westerlies Across Different Ocean Basins. *Geophys. Res. Lett.,* **47,** e2020GL088890 (2020).

43. Jones, R. W., Renfrew, I. A., Orr, A., Webber, B. G. M., Holland, D. M., Lazzara, M. A. Evaluation of four global reanalysis products using in situ observations in the Amundsen Sea Embayment, Antarctica. *J. Geophys. Res. Atmos.* **121** (11), 6240-6257 (2016).
44. Gelaro, R. et al. The Modern-Era Retrospective Analysis for Research and Applications, Version 2 (MERRA2). *J. Clim.* **30** (14), 5419-5454 (2017).
45. Kobayashi, S. et al. The JRA-55 Reanalysis: general specifications and basic characteristics. *J. Met. Soc. Japan* **93** (1), 5-48 (2015).
46. Thompson, D. W. J., et al., Signatures of the Antarctic ozone hole in Southern Hemisphere surface climate change. *Nat. Geosci.*, **4,** 741–749 (2011).
47. Polvani, L. M., Waugh, D. W., Correa, G. J. P., Son, S. Stratospheric ozone depletion: the main driver of twentieth-century atmospheric circulation changes in the Southern Hemisphere. *J. Clim.* **24** (3), 795-812 (2011).
48. Deser, C., Guo, R. X. & Lehner, F. The relative contributions of tropical Pacific sea surface temperatures and atmospheric internal variability to the recent global warming hiatus. Geophys. Res. Lett. **44,** 7945–7954 (2017).
49. Lachlan-Cope, T. A., Connolley, W. M., Turner, J. The role of the non-axisymmetric Antarctic orography in forcing the observed pattern of variability of the Antarctic climate. *Geophys. Res. Lett.* **28** (21), 4111-4114 (2001).
50. Bracegirdle, T. J. et al. Improvements in circumpolar Southern Hemisphere extratropical atmospheric circulation in CMIP6 compared to CMIP5. *Earth and Space Sci.* **7,** e2019EA001065 (2020).
51. Turner, J., Phillips, T., Hosking, J. S., Marshall, G. J., Orr, A. The Amundsen Sea low. *Int. J. Climat.* **33,** 1818-1829 (2013).
52. Schneider, D. P., Steig, E. J. Ice cores record significant 1940s Antarctic warmth related to tropical climate variability. *Proc. Natl Acad. Sci.* **105** (34), 12154-12158 (2008).
53. Smith, J. A. et al. Sub-ice-shelf sediments record history of twentieth-century retreat of Pine Island Glacier. *Nature* **541,** 77-80 (2017).
54. Freund, M. B. et al. Higher frequency of Central Pacific El Niño events in recent decades relative to past centuries. *Nat. Geosci.* **12,** 450-455 (2019).
55. Grothe, P. R. et al. Enhanced El Niño-Southern Oscillation variability in recent decades. *Geophys. Res. Lett.* **46,** e2019GL083906 (2019).
56. Nakayama, Y., Menemenlis, D., Zhang, H., Schodlok, M., Rignot, E. Origin of Circumpolar Deep Water intruding onto the Amundsen and Bellingshausen Sea continental shelves. *Nat. Comm.* **9,** 3403 (2018).
57. PAGES 2k Consortium. A global multiproxy database for temperature reconstructions of the Common Era. *Sci. Data* **4,** 170088 (2017).
58. Thomas, E. R. et al. Regional Antarctic snow accumulation over the past 1000 years. *Clim. Past* **13,** 1491-1513 (2017).

59. Sanchez, S. C., Hakim, G. J., Saenger, C. P. Climate model teleconnection patterns govern the Niño 3.4 response to early 19th century volcanism in coral-based data assimilation reconstructions. *J. Clim.* Preprint at https://journals.ametsoc.org/view/journals/clim/aop/JCLI-D-20-0549.1/JCLI-D-20-0549.1.xml (2021).
60. Hansen, J., Ruedy, R., Sato, M., Lo, K. Global surface temperature change, Rev. *Geophys.* **48,** RG4004 (2010).
61. Schneider, U., Becker, A., Finger, P., Meyer-Christoffer, A., Ziese, M., and Rudolf, B. GPCC's new land surface precipitation climatology based on quality-controlled in situ data and its role in quantifying the global water cycle. *Theor. Appl. Climatol*. **115,** 15–40 (2014).
62. Bretherton, C. S., Widmann, M., Dymnikov, V. P., Wallace, J. M. & Bladé, I. The effective number of spatial degrees of freedom of a time-varying field. *J. Clim.* **12,** 1990-2009 (1999).
63. Nash, J., and Sutcliffe, J. River flow forecasting through conceptual models: Part I- A discussion of principles, *J. Hydrol.* **10** (3), 282 – 290 (1970).
64. Bracegirdle, T. J. et al. Assessment of surface winds over the Atlantic, Indian, and Pacific Ocean sectors of the Southern Ocean in CMIP5 models: historical bias, forcing response, and state dependence. *J. Geophys. Res. Atmos.* 118, 547-562 (2013).
65. Kidston, J. and Gerber, E. P. Intermodel variability of the poleward shift of the austral jet stream in the CMIP3 integrations linked to biases in 20th century climatology. *Geophys. Res. Lett.* **37** (9) L09708 (2010).
66. Barnes, E. A. and Polvani, L. Response of the Midlatitude Jets, and of Their Variability, to Increased Greenhouse Gases in the CMIP5 Models. *J. Clim.* **26,** 7117-7135 (2013).

Figures

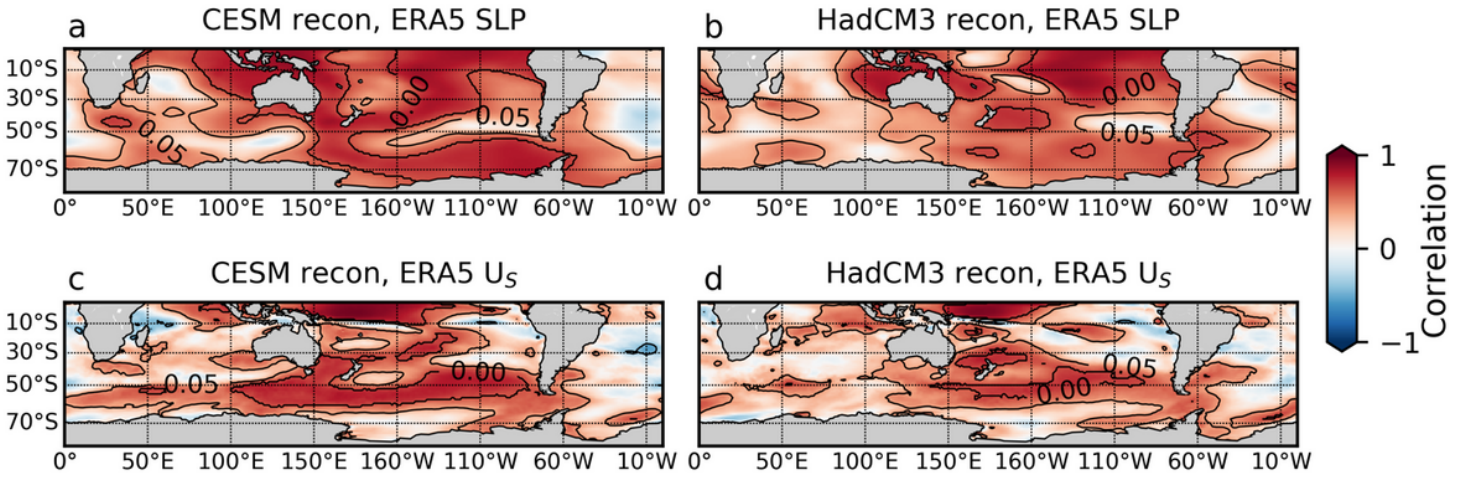

Figure 1

Spatial correlations between reconstructions and ERA5. a, Correlations between sea level pressure (SLP) in ERA5 and the CESM reconstruction for the period 1979-2005. b, Same as a, but with the HadCM3 reconstruction. c, d, Same as top row, but for zonal surface wind (US). Contour spacing is 0.05. Reconstructions are generated with all proxies. See Figs. S1 and S2 for coefficient of efficiency and calculations with NCEP2.

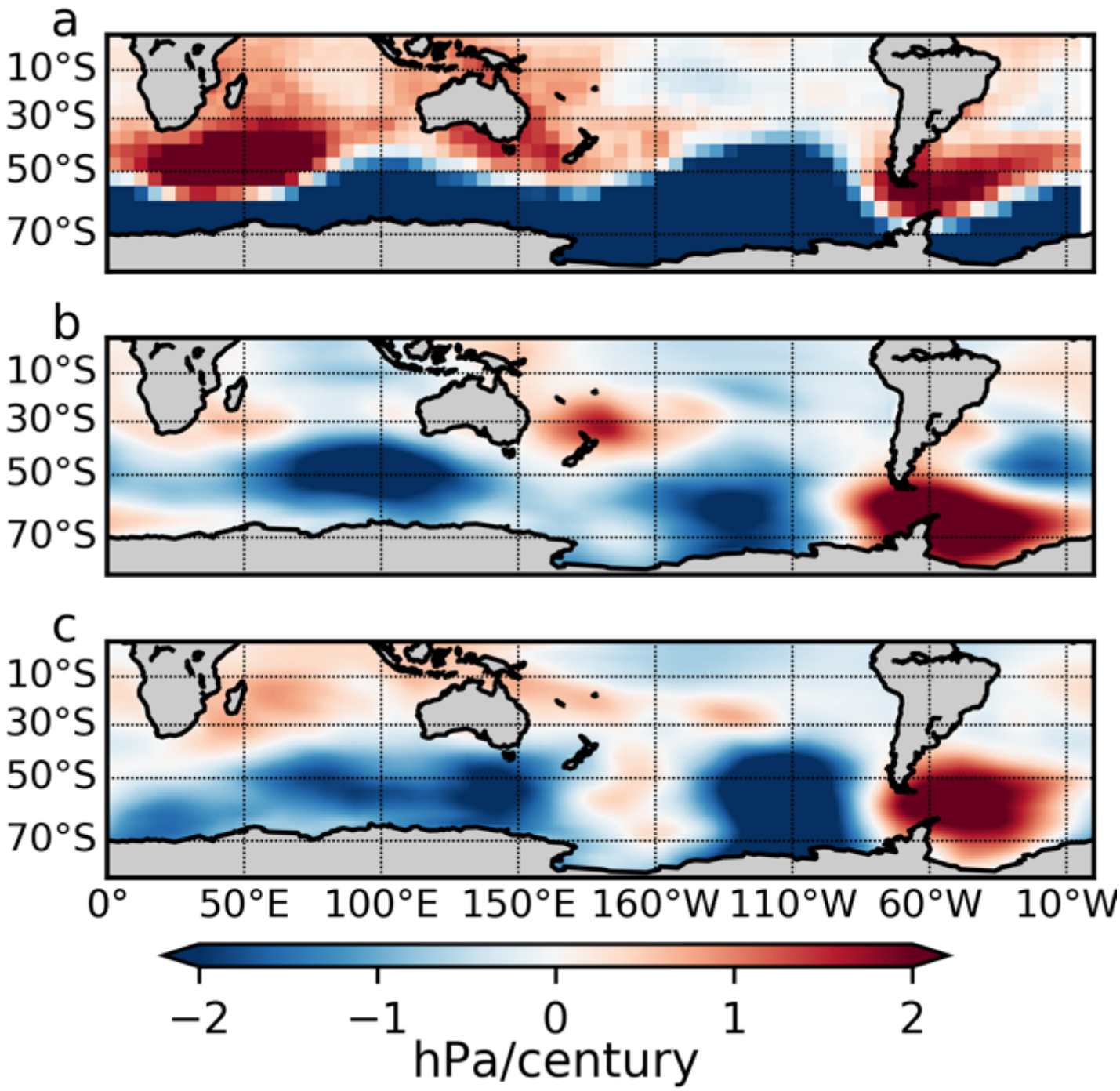

Figure 2

Trends in sea level pressure from 1951-2004. a, Trends in HadSLP2 observations. b, Trends in the CESM reconstruction. c, Trends in the HadCM3 reconstruction. Reconstructions are generated with all proxies.

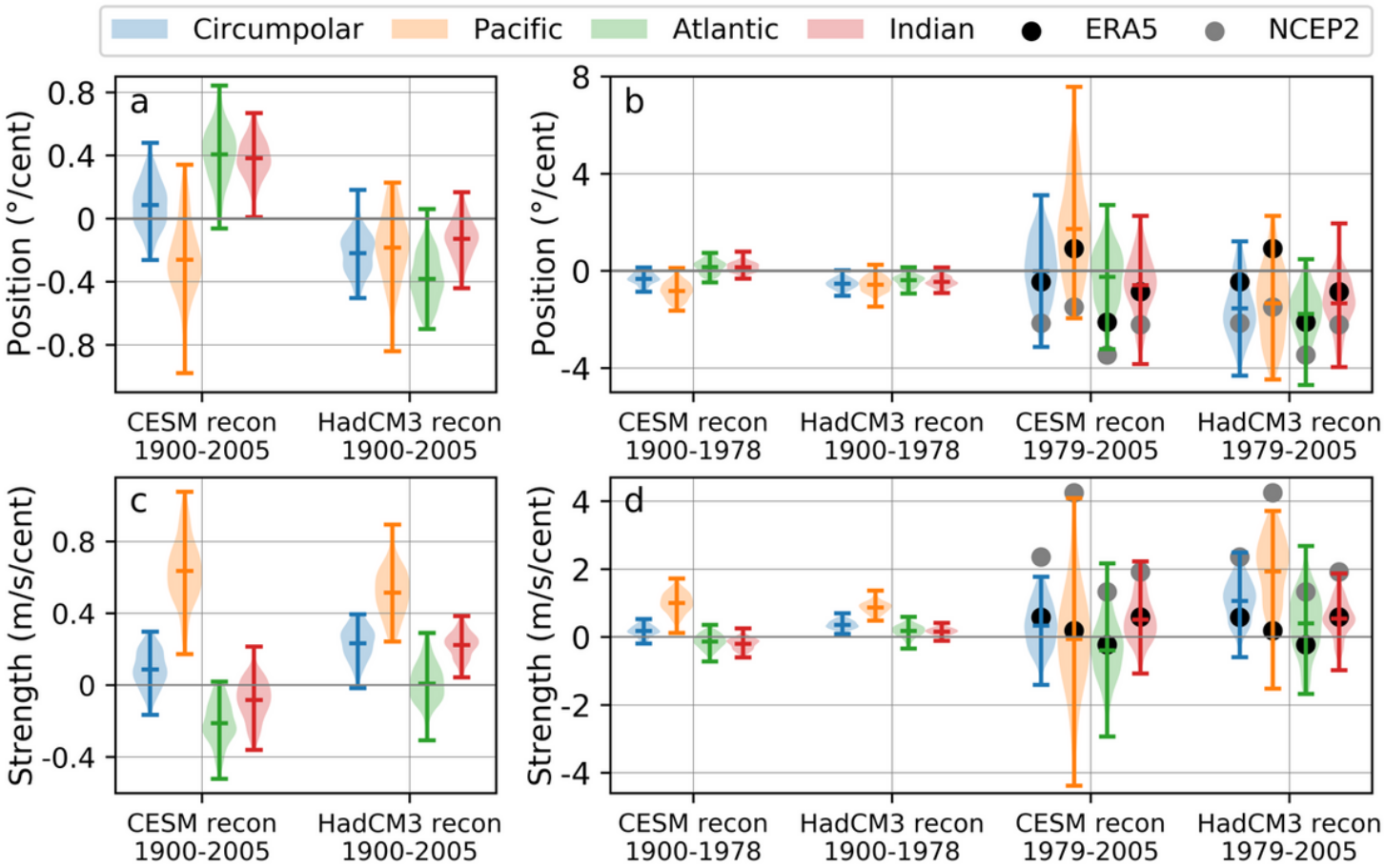

Figure 3

Trends in Southern Hemisphere surface westerly position and strength. a, Violin plots of the distribution of trends in position for the period 1900-2005, calculated using 100 random draws from ensemble members of the CESM reconstruction and the HadCM3 reconstruction (Methods), both made with assimilation of all proxy records. Horizontal lines on the violin plots represent the range of trends and the mean, and the shading represents the probability distribution. Trends are given for the zonally averaged circumpolar westerly winds (blue), as well as for three sectors of the wind belt: the Pacific (orange, 150–290°E), Atlantic (green, 290–20°E), and Indian (red, 20–150°E) Ocean sectors. b, Trends in position during the pre-satellite era and satellite era. For the satellite era (1979-2005), trends from ERA5 and NCEP2 are also given, represented by dots. c, Same as in a, but for strength. d, Same as in b, but for strength. Trend magnitudes and their 2 standard deviation uncertainties (Methods) are shown in Table S3.

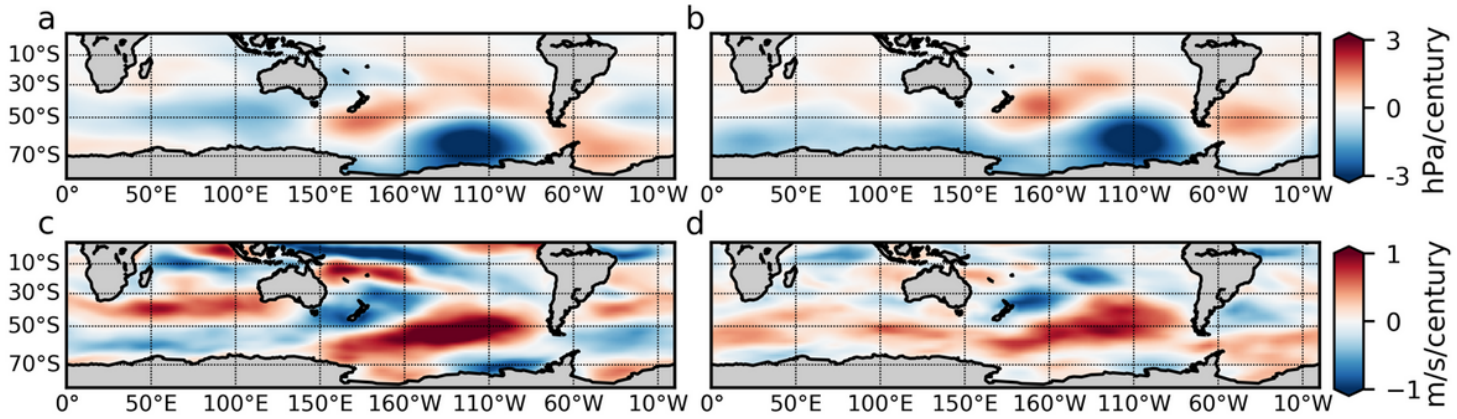

Figure 4

Reconstructed trends in sea level pressure (SLP) and zonal surface winds (US) from 1900-2005. a, SLP trends in the CESM reconstruction. b, SLP trends in the HadCM3 reconstruction. c, US trends in the CESM reconstruction. d, US trends in the HadCM3 reconstruction. Reconstructions are generated with all proxies.

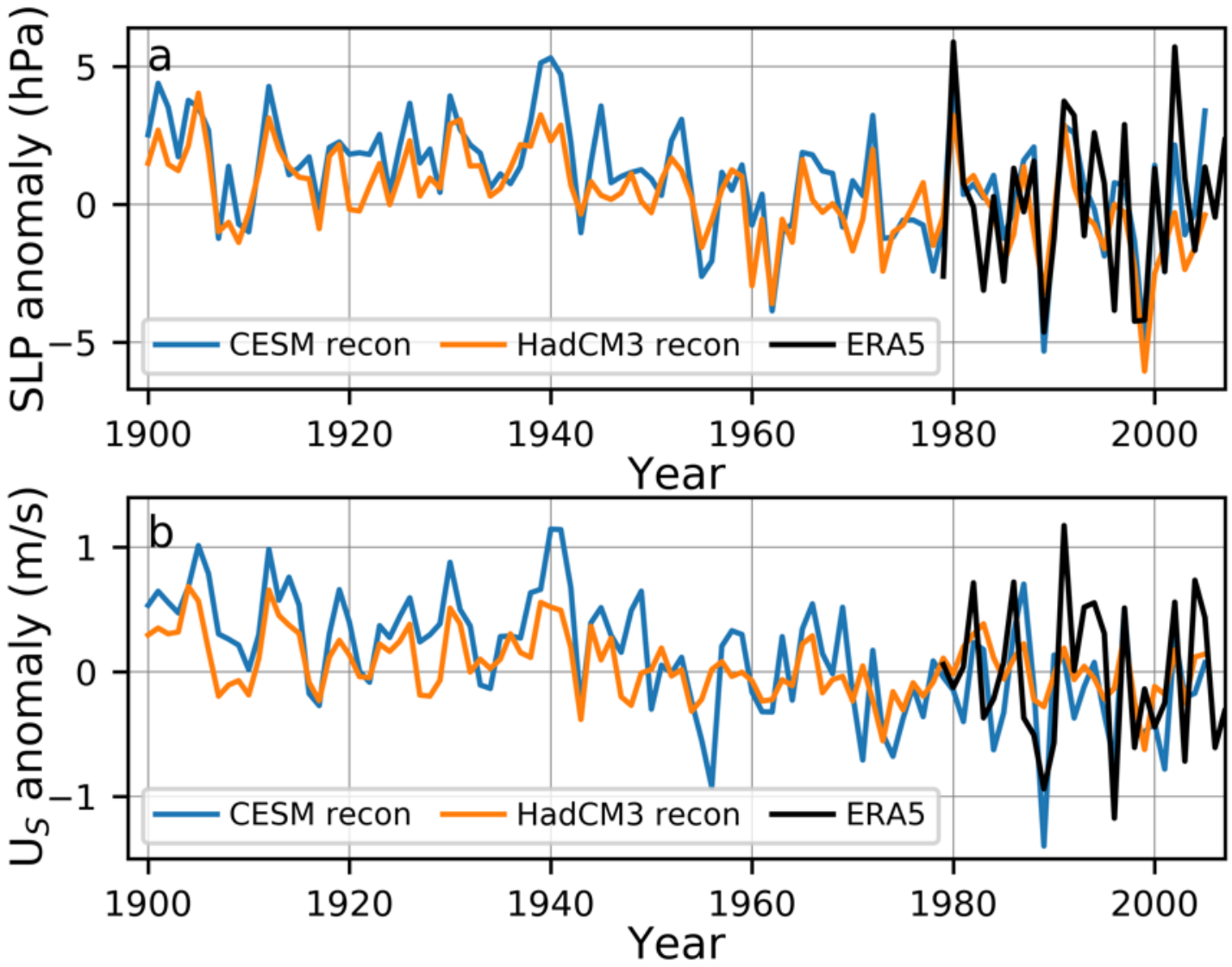

Figure 5

Sea level pressure (SLP) and zonal surface wind (US) anomalies in the Amundsen Sea continental shelf break region from 1900-2005. a, Time series of annual SLP anomalies in the CESM reconstruction and HadCM3 reconstruction, generated with all proxies, averaged over the region 70-72°S, 102-115°W. The same calculation in ERA5 is also shown, from 1979-2005 (Correlation with ERA5 r = 0.74, 0.57, p-values < 0.01; for CESM reconstruction and HadCM3 reconstruction, respectively). b, Same as in a, but for US (r = 0.54, 0.49, p-values < 0.05). Anomaly reference period is 1979-2005.

Supplementary Files

This is a list of supplementary files associated with this preprint. Click to download.

- Supplement.docx